

Multistatic Uniform Diffraction Tomography Derived Structural-Prior in Bayesian Inversion Framework for Microwave Tomography

Adel Omrani, Rahul Yadav, Guido Link, Timo Lähivaara, Marko Vauhkonen, and John Jelonnek

Abstract—In this work, a quantitative Bayesian inversion framework for microwave tomography (MWT) is coupled with a multistatic uniform diffraction tomography (MUDT) method to improve the imaging quality. The method is applied for an industrial use-case of MWT in which we estimate the 2-D spatial distribution of moisture (in terms of dielectric constant) in a polymer foam. In essence, we modify the prior information in the single-frequency Bayesian inversion framework using high-resolution complementary structural information of the imaging domain from a qualitative approach MUDT utilizing broadband frequency-domain data. This way of obtaining structural prior information is effective as it utilizes the data from the same microwave sensor setup in contrast to the frequency-hopping approach, priors derived for other imaging modalities or radar-based techniques with the co-located sensor using, for example, uniform diffraction tomography (UDT) inversion framework. Proposed algorithm performance is tested for different moisture scenarios in the polymer foam with 3D numerical and experimental data from our developed MWT system. It is shown that the proposed approach significantly improves the reconstruction accuracy for the considered cases over just using the Bayesian inversion approach.

Index Terms—microwave tomography, non-linear optimization, statistical inverse problems, structural prior, multistatic uniform diffraction tomography, Green’s function

I. INTRODUCTION

MICROWAVE tomography in industrial process applications [1] includes food inspection [2], detection of multi-phase flow [3], monitoring of moisture in stored grain bin [4], among many other. A new application of MWT is in the industrial microwave heating system known as HEP-HAISTOS [5] for the purposes of monitoring and intelligent control of distributed microwave power sources (magnetrons). Applications of this microwave heating technology is in the

Submitted: October 13, 2022. This work has been supported by the European Union’s Horizon 2020 Research and Innovation Program under the Marie Skłodowska-Curie grant agreement No. 764902. (TOMOCON-www.tomocon.eu). The work is also supported by the Academy of Finland (Finnish Centre of Excellence of Inverse Modelling and Imaging, project number 312344, and project number 321761).

Adel Omrani and Guido Link are with the Institute for Pulsed Power and Microwave Technology, Karlsruhe Institute of Technology (KIT), 76344 Eggenstein-Leopoldshafen, Germany (e-mail: adel.hamzekalaei@kit.edu; guido.link@kit.edu).

Rahul Yadav, Timo Lähivaara and Marko Vauhkonen are with the Department of Applied Physics, University of Eastern Finland, 70210 Kuopio, Finland (e-mail: rahuly@uef.fi; timo.lahivaara@uef.fi; marko.vauhkonen@uef.fi).

John Jelonnek is with the Institute for Pulsed Power and Microwave Technology, 76344 Eggenstein-Leopoldshafen; and Institute of Radio Frequency Engineering and Electronics, Karlsruhe Institute of Technology, 76131 Karlsruhe, Germany (e-mail: john.jelonnek@kit.edu).

areas of drying porous and non-porous materials, sintering of ceramics and processing of carbon fibers [6]. In drying applications, the goal is to maintain a stable product output moisture level.

Generally, in this system, feedback control allows manipulation of the temperature distribution in the material to prevent over-heating and thermal-runaway situation [5]. However, temperature based feedback control may not provide sufficient and stable control in drying applications as the loss factor of the material is also dependent on moisture content [7] that may result in uneven levelling and undesired moisture level at the the output. More so, non-uniform moisture distribution (i.e., wet-spots surrounded by low moisture areas) may aggravate the situation of uneven drying. The process efficiency can be improved by use of the spatial moisture distribution as measured and controlled variable in the intelligent controller design [8]. Therefore, integration of MWT operating in X-band (from 8 GHz to 12 GHz) was proposed [9], [10]. Based on the estimated spatial moisture information from MWT, the control unit can tune the power of the distributed microwave sources, pulse duration and achieve desired uniform moisture level. In this article, the focus is on assessing the feasibility of the MWT reconstruction algorithm and hence related control strategies are not discussed.

Our goal is to estimate both location and dielectric value of the moisture wet-spot(s) in a polymer foam using a MWT sensor setup. For image reconstruction, we propose a coupled approach in which, at the first step, a qualitative framework based on an extended version of uniform diffraction tomography (UDT), called multistatic uniform diffraction tomography (MUDT) [11], is performed with multi-view, multistatic and multifrequency scattering data obtained in X-band to localize the wet-spots. In MUDT, the location of an object inside the imaging domain is determined by the linear relationship between the relative complex permittivity function and the received signal in the spectral domain. And in comparison to UDT [12], [13], the MUDT approach i) eliminates the need for mechanical scanning of the sensor, ii) provides aliasing-free images by following Nyquist sampling criteria, and can resolve multiple targets with significant improvement in the spatial resolution. At the second step, the retrieved information from MUDT is segmented into regions of dry part and approximate moisture wet-spot(s) and used to form prior covariance structure in qualitative Bayesian inversion framework operating with single frequency data. The prior model is also known as structural prior information [14]–

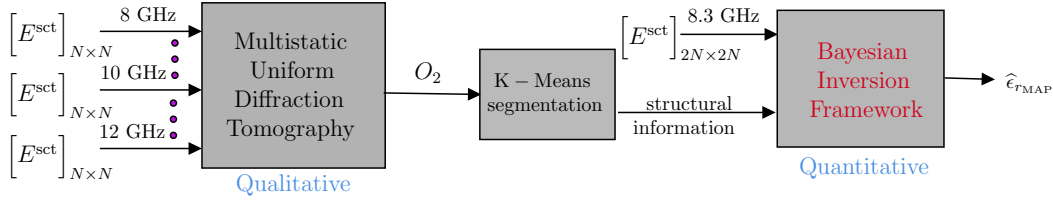


Fig. 1: General framework of the proposed method.

[16]. Figure 1 represents the idea of the proposed method in a nutshell. Proposed algorithm performance is tested for different moisture scenarios in the polymer foam with 3-D numerical and experimental data from our developed MWT system. Results presented show the efficacy of this approach over just the qualitative approach with smoothness prior [17] to achieve good reconstruction accuracy.

In frequency-domain MWT, similar ideas on using structural prior knowledge to improve the reconstruction accuracy are reported in biomedical applications in [18]–[20]. In these articles, the structural prior information is extracted from other imaging modalities, say e.g. from ultrasound, MRI, etc, and used in the construction of prior in MWT imaging algorithm. In our industrial imaging case, considering overall system cost, employing a dual-imaging modality can be critical. To avoid dual imaging setup, alternative strategies based on radar-based regional-imaging [21], [22] have been studied and have proven very effective in improving the image quality. However, the aforementioned technique utilises mono-static scanning configuration for data acquisition which is again time-consuming. Using the available electromagnetic measurements (i.e., the same setup) to form structural prior information is gaining pace and has been tested with algorithms in time-domain [23], [24], and frequency-domain [25], [26]. Our work is a contribution in this direction. This article is organized in the following format. Section II details the MUDT qualitative method, and quantitative Bayesian inversion framework. Section III discusses the incorporating of structural smoothness prior to the Bayesian framework. Section IV contains the numerical assessment, and experiment results are provided in section V. Finally, Section VI shows the concluding remarks.

II. THEORY

For simplicity, the formulation here is represented for a 2-D case assuming no variation in x-direction ($\frac{\partial}{\partial x} = 0$). The 2-D configuration of the multistatic microwave tomography system, studied in this work is illustrated in Fig. 2 with antenna array located on top and bottom of the foam, respectively. The free space is represented as layer ① and ③ and the foam is represented as layer ② with a random embedded irregularities denoted by Ω_h . In free space, the relative dielectric constant is denoted as $\epsilon_{r,1}$ whereas the relative dielectric constant of the foam is set to $\epsilon_{r,2}$, and dielectric constant of the irregularity is set to $\epsilon_{r,i}$. The distance of the top and bottom antenna to the top and bottom of the polymer foam is $t_1 = t_3$, and layer ② has thickness t_2 . Next, we discuss the qualitative and quantitative reconstruction approaches in more detail.

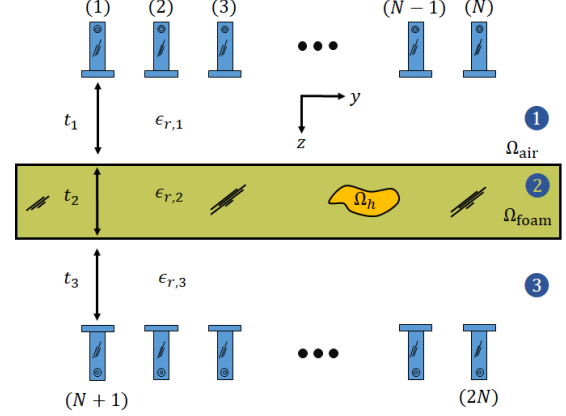


Fig. 2: Schematic of the free-space MWT setup used in this study.

Throughout the paper, harmonic time-convention $e^{-j\omega t}$ is assumed and suppressed, where ω is the angular frequency, and $j = \sqrt{-1}$.

A. Multistatic UDT: structural information of the target

Considering only the top antennas and under the assumption of the point source as a transmitter, the scattered electric field at the receiver position due to the irregularities in the layer ②, can be modeled in the following integral form [27]

$$E^{\text{sct}}(\vec{r}_r, \vec{r}_t, k) = k_0^2 \int_{\Omega_{\text{foam}}} G_{\text{eb}}^{(21)}(\vec{r}_r, \vec{r}', k) O_2(\vec{r}', k) E_2^{\text{tot}}(\vec{r}', \vec{r}_t, k) d\vec{r}', \quad (1)$$

where $E_2^{\text{tot}}(\vec{r}', \vec{r}_t, k)$ is the total electric field in layer ② and $E^{\text{sct}}(\vec{r}_r, \vec{r}_t, k)$ represents the received scattered at the antennas position. The vectors $\vec{r}_r = (y_r, z_r)$ and $\vec{r}_t = (y_t, z_t)$ represent the observation and source points, respectively. $O_2(\vec{r}', k) = (\epsilon_{r,i}(\vec{r}') - \epsilon_{r,2})$ is the relative dielectric constant of the irregularity. $\epsilon_{r,i}(\vec{r}')$ is the profile of the dielectric constant of the irregularity (wet-spots) and k_0 is the wavenumber in the free space. $\Omega_{\text{foam}} \subset \mathbb{R}^2$ is the region of interest which is in our case layer ② and $\vec{r}' \in \Omega_{\text{foam}}$. $G_{\text{eb}}^{(21)}(\vec{r}_r, \vec{r}_t, k)$ is the electric background (media without any irregularities inside) Green's function. The superscript (21) denotes that the source point is located in layer ① and the observation point is in layer ②.

By applying the first-order Born approximation [28], the total electric field E_2^{tot} can be replaced by the background electric field of the layer ②. Due to the excitation by a point source the electric field can be replaced by the Green's

function [29] and also using the symmetry property of Green's function [30], a multistatic model for the scattering electric field can be expressed as

$$E^{\text{sct}}(\vec{r}_r, \vec{r}_t, k) \approx k_0^2 \int_{\Omega_{\text{foam}}} G_{\text{eb}}^{(21)}(\vec{r}_r, \vec{r}', k) O_2(\vec{r}', k) G_{\text{eb}}^{(21)}(\vec{r}', \vec{r}_t, k) d\vec{r}'. \quad (2)$$

The spectral representation of the Green's function in layer ② (modeled by the incident field in that layer) when the point source is located in layer ① is [27]

$$G_{\text{eb}}^{(21)}(\vec{r}, \vec{r}_t, k) = \frac{1}{\pi} \int_{-\infty}^{+\infty} \tilde{T}_2(k_y, k_z) \frac{e^{-jk_z z}}{k_{z1}} e^{-jk_y(y - y_t)} dk_y, \quad (3)$$

if $z > 0$ and $\text{Im}(k_2^2 - k_y^2)^{\frac{1}{2}} < 0$. $\tilde{T}_2(k_y, k_z)$ is the transmission coefficient in layer ② and can be obtained by applying the continuity conditions between layers for the transverse magnetic field in x-direction (TM_x) [27]. k_y and k_z are wavenumbers in y and z-directions. The dispersion relation in the layer ① ($l = 1, 2, 3$) is expressed by $k_{zl} = \sqrt{k_l^2 - k_y^2}$, and $k_l = k_0 \sqrt{\epsilon_{r,l}}$ is the wavenumber in layer ① while k_0 is the free-space wavenumber. By substituting (3) in (2), the

$$O_2(y, z) \approx \frac{\int_{\omega} \int_{-\infty}^{+\infty} \frac{k_{z1}''}{k_2^2} \frac{1}{|\tilde{T}_2|^2} \frac{k_2}{\omega k_{z2}''} e^{+j \left[k_{z2}'' z + \angle \tilde{T}_2 \left(\frac{k_y''}{2}, k_{z2}'', t_l \right) + \frac{k_y''}{2} (y_t - y_r) + \frac{\pi}{4} \right]}{2\sqrt{\pi} \int_{\omega} \int_{-\infty}^{+\infty} \frac{k_2}{\omega k_{z2}''} \frac{1}{\sqrt{\frac{k_2^2}{k_{z2}^3} z + \frac{\partial^2}{\partial k_y^2} [\angle \tilde{T}_2]_{k_y = \frac{k_y''}{2}}}} dk_y'' d\omega} \tilde{E}_2^{\text{sct}}(k_y'', \omega) e^{jk_y'' y} dk_y'' d\omega \quad (5)$$

B. Quantitative method: Bayesian inversion framework

Consider an inverse problem of identifying an unknown parameter $\epsilon_r \in \mathbb{C}$ given noisy measurement data $E^{\text{sct}} \in \mathbb{C}$ according to the observation model

$$E^{\text{sct}} = \mathcal{F}(\epsilon_r) + \xi, \quad (6)$$

where $\mathcal{F}: \epsilon_r \rightarrow E^{\text{sct}}$ is the forward model as represented by (1), that maps $\epsilon_r = \epsilon_r' - j\epsilon_r''$ to the measurement, and ξ denotes the additive measurement noise component. The unknown parameter and noise terms are considered mutually independent. Note that the measurement data and unknown parameters are complex quantities, therefore in the present study the real and imaginary parts are treated as real variables for the optimisation problem.

In the Bayesian framework the unknown parameters are treated as random variables, and information about them are expressed in terms of probability densities. The inverse problem is then expressed as given the measured scattering data, the task is to find the conditional probability density $\pi(\epsilon_r | E^{\text{sct}})$ for the unknown parameter ϵ_r . The conditional probability density is constructed using the Bayes' theorem as

$$\pi(\epsilon_r | E^{\text{sct}}) = \frac{\pi(E^{\text{sct}} | \epsilon_r) \pi(\epsilon_r)}{\pi(E^{\text{sct}})} \propto \pi(E^{\text{sct}} | \epsilon_r) \pi(\epsilon_r), \quad (7)$$

2-D multistatic model for the received electric field can be obtained as

$$E^{\text{sct}}(\vec{r}_r, \vec{r}_t, k) \approx \frac{k_0^2}{\pi^2} \int_{\Omega_{\text{foam}}} O_2(y', z', k) \int_{-\infty}^{+\infty} \int_{-\infty}^{+\infty} dk_y dk_y' \frac{|\tilde{T}_2(k_y) \tilde{T}_2(k_y')|}{k_{z1} k_{z1}'} \cdot e^{-j \left[(k_y + k_y') y' - k_y y_r - k_y' y_t \right]} \cdot e^{-j \left[(k_{z2} + k_{z2}') z' - \angle \tilde{T}_2(k_{z2}) - \angle \tilde{T}_2(k_{z2}') \right]} d\Omega'_{\text{foam}}. \quad (4)$$

where \angle is the phase. The relative complex permittivity function can be determined from (4) by changing variables to $k_y'' = k_y + k_y'$ and using 2-D spatial Fourier transform definition for the received signal. After some straightforward calculation, a closed form expression for O_2 can be obtained as given in (5) [12], [13].

In (5), $\tilde{E}_2^{\text{sct}}(k_y'', \omega)$ is the spatial Fourier transform of the received scattered field. The relative complex permittivity function gives the domain of the irregularities in the 2-D cross-section of the imaging region of interest which is the polymer foam denoted by Ω_{foam} . Spatial prior information will be formed using this reconstructed image.

where $\pi(\epsilon_r | E^{\text{sct}})$ is the posterior density, $\pi(E^{\text{sct}} | \epsilon_r)$ is the likelihood density which represents the distribution of the measured data if ϵ_r is known, and $\pi(\epsilon_r)$ is the prior density which contains the prior information available for unknown ϵ_r . The denominator is the marginal density of the measured data and plays the role of normalization constant. It is often ignored since it requires integration over all possible ϵ_r .

The likelihood density, if the noise is assumed to be additive Gaussian with zero mean with the covariance matrix Γ_{ξ} , can be written as [31]

$$\pi(E^{\text{sct}} | \epsilon_r) \propto \exp \left\{ -\frac{1}{2} \|L_{\xi}(E^{\text{sct}} - \mathcal{F}(\epsilon_r))\|^2 \right\}, \quad (8)$$

where L_{ξ} is the Cholesky factor of the inverse of the noise covariance matrix and $(\cdot)^{\top}$ denotes the transpose operator. As prior information, it is first assumed that the moisture variation is smooth inside the foam. This indicates that unknowns have a natural neighborhood structure i.e two adjacent values should differ from each other only moderately. Such an assumption can be encoded using a Gaussian prior model [32] with mean η_{ϵ_r} and covariance Γ_{ϵ_r} as

$$\pi_{\text{smooth}}(\epsilon_r) \propto \exp \left\{ -\frac{1}{2} \|L_{\epsilon_r}(\epsilon_r - \eta_{\epsilon_r})\|^2 \right\}. \quad (9)$$

Here, L_{ϵ_r} is a Cholesky factor of the inverse of the prior covariance matrix Γ_{ϵ_r} . The prior covariance matrix encodes the spatial smoothness knowledge of the unknowns.

The posterior density in (7) contains the complete solution of the inverse problem in the Bayesian framework and can be expressed by point estimates. One of the most common point estimate is the *maximum a posteriori* (MAP). The MAP estimate can be computed from the posterior as

$$\hat{\epsilon}_{r\text{MAP}} = \arg \max_{\epsilon_r} \pi(\epsilon_r | E^{\text{sct}}). \quad (10)$$

This problem is equivalent to the minimization problem [32], [33], [34]

$$\hat{\epsilon}_{r\text{MAP}} = \arg \min_{\epsilon_r} \{ \|L_{\xi}(E^{\text{sct}} - \mathcal{F}(\epsilon_r))\|^2 + \|L_{\epsilon_r}(\epsilon_r - \eta_{\epsilon_r})\|^2 \}, \quad (11)$$

which is a regularized non-linear least square (LS) problem. This minimization problem can be formally solved using a gradient based optimization method. In the Newton type method the minimum point is found iteratively by linearizing the forward model, resulting in linear LS solution in each iteration as

$$\epsilon_{r\ell+1} = \epsilon_{r\ell} + \alpha_{\ell} A^{-1} B, \quad (12)$$

with,

$$A = (J_{\ell}^T \Gamma_{\xi}^{-1} J_{\ell} + \Gamma_{\epsilon_r}^{-1}), \quad (13a)$$

$$B = (J_{\ell}^T \Gamma_{\xi}^{-1} (E^{\text{sct}} - \mathcal{F}(\epsilon_{r\ell})) - \Gamma_{\epsilon_r}^{-1} (\epsilon_{r\ell} - \eta_{\epsilon_r})), \quad (13b)$$

where α_{ℓ} is the step length parameter, index ℓ is the iteration number. The term J is a Jacobian matrix (its derivation can be found in [35]) which is decomposed in real and imaginary parts as

$$J = \begin{bmatrix} J_{\mathbb{R}} & J_{\mathbb{I}} \\ -J_{\mathbb{I}} & J_{\mathbb{R}} \end{bmatrix}_{2S \times 2N_n} \quad (14)$$

where S is the total number of measurements and N_n is the total number of unknowns in the cross-section of the foam domain.

1) *Noise model*: Let us denote the noise standard deviation (STD) of the real and imaginary parts of the complex-valued scattered field data to be $\sigma_{\mathbb{R}}$ and $\sigma_{\mathbb{I}}$, respectively. Under the assumption that noise between measurement points are independent and not correlated, the noise covariance is then given as

$$\Gamma_{\xi} = \begin{bmatrix} \sigma_{\mathbb{R}}^2 \odot \mathbf{I}_S & 0_S \\ 0_S & \sigma_{\mathbb{I}}^2 \odot \mathbf{I}_S \end{bmatrix}, \quad (15)$$

where \mathbf{I}_S is an $S \times S$ identity matrix and 0_S is an $S \times S$ zero matrix and \odot is the Hadamard operator. In the case of real measurements, the noise covariance can be estimated by performing repeated measurements [36].

2) *Smoothness Prior*: In this case the moisture field variation in the entire foam is assumed to be smooth. Here, such a random field is generated using a multivariate Gaussian distribution with anisotropic covariance structure C [17] which can account for the inhomogeneities in the unknown in terms of the characteristic length parameter. In practice, the characteristic

length affect the moisture distribution in y, and z-directions. The elements of the covariance C can be calculated as

$$C_{ij} = \exp \left(-\frac{\|y_i - y_j\|^2}{c_y^2} - \frac{\|z_i - z_j\|^2}{c_z^2} \right), \quad (16)$$

where $i, j = 1, \dots, N_n$ and c_y, c_z are the characteristic lengths (CL) components. If real and imaginary parts of the dielectric constant are assumed uncorrelated, the prior covariance matrix can be written as

$$\Gamma_{\epsilon_r} = \begin{pmatrix} \Gamma_{\epsilon_r'} & 0 \\ 0 & \Gamma_{\epsilon_r''} \end{pmatrix} = \begin{bmatrix} \sigma_{\epsilon_r'}^2 C & 0_{N_n} \\ 0_{N_n} & \sigma_{\epsilon_r''}^2 C \end{bmatrix}_{2N_n \times 2N_n}, \quad (17)$$

where 0_{N_n} is an $N_n \times N_n$ zero matrix, and $\sigma_{\epsilon_r'}$, and $\sigma_{\epsilon_r''}$ are the standard deviations for the real and imaginary parts of dielectric constant, respectively. Note here that the standard deviations terms control the amplitude of real and imaginary parts of dielectric constant in the prior covariance matrix. These values can be determined using the dielectric characterisation of the foam which is described in details in [31], [37]. The moisture field variation in terms of real part of dielectric constant can be expressed as [38]

$$\epsilon_r' = \eta_{\epsilon_r'} \mathbf{1} + \sigma_{\epsilon_r'} LZ, \quad (18)$$

where $\mathbf{1}$ is all-ones vector, L is the lower triangular matrix of the Cholesky factorization of the covariance C , and Z is a standard normal random vector. Similarly, imaginary part can also be expressed.

III. STRUCTURAL SMOOTHNESS PRIOR

In the smoothness priors, generally it is assumed that the coupling between the neighboring entries is same everywhere. It is not uncommon, however, to have spatial structural information about the unknown; this information can be encoded into the prior by accounting for the fact that the solution may jump across structure boundaries, while being smooth within each structure. Knowledge about the structure may come from different sources [15] carrying complementary information about the structure of the scatterers or their location inside the imaging domain.

In the present study, we propose to use the structural knowledge about the domain from MUDT that conveys the location of moisture wet-spots inside the foam. In order to encode this structural information in the existing smoothness prior model, varying degree of smoothness is applied in different regions i.e., in the dry part and inside the support domain of the wet-spots. Here, the approximate support domain of the moisture wet-spots and the dry region are deduced using K-means segmentation. To achieve different degree of smoothness, CL components and standard deviations terms are chosen separately for dry and wet-spots regions. Therefore, the prior covariance matrix is modified as

$$C_{ij} = \begin{cases} C_{ij}(c_{y1}, c_{z1}) & \forall i, j \in \Omega_d \\ C_{ij}(c_{y2}, c_{z2}) & \forall i, j \in \Omega_h, \end{cases} \quad (19)$$

where Ω_h and Ω_d represent approximated wet-spot and dry part regions, respectively. Large CL along with small amplitude (standard deviation) in the dry part will constraint

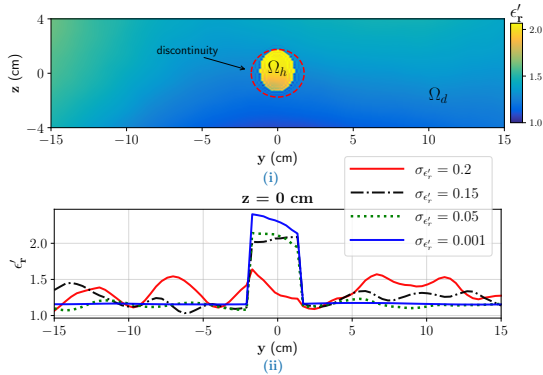


Fig. 3: (i) A sample realization from the structural-prior model derived using MUDT. (ii) Effect of values of $\sigma_{\epsilon'_r} \in \Omega_d$ in the sample realization.

the estimate to have constant neighbourhood structure in the domain. This is equivalent of assuming that pixel elements are more correlated in the dry regions.

Sample realization from the structural prior model using (18), when one wet-spot is assumed to be detected from the MUDT reconstruction, is shown in Fig. 3 (i). More details of the MUDT reconstruction are provided in the next Section, see Fig. 4(i). For the drawn sample, in the dry part domain (Ω_d), CL of $c_{y_1} = 30$ cm, and $c_{z_1} = 8$ cm and $\sigma_{\epsilon'_r} = 0.15$ are assumed and for the wet-spot a CL $c_{y_2} = 3$ cm, and $c_{z_2} = 3$ cm and $\sigma_{\epsilon'_r} = 0.5$ are assumed with a mean value of $\eta_{\epsilon'_r} = 1.16$. As can be clearly seen, in the dry part the smoothness is varying slowly due to the large CL and in the approximate wet-spots region the variation is approximately constant. Also, we have plotted the data on the cross-section line $z = 0$ cm for different variance terms and constant correlation lengths in the dry part and is shown in Fig. 3 (ii). It can be seen that a smaller variance provides a more realistic coupling between the neighboring entries in the Ω_{foam} . The above strategy to generate the structural prior can be extended to N numbers of scatterers (wet-spots) in the domain.

IV. NUMERICAL ASSESSMENT

This section is devoted to first numerically evaluate the performance of the proposed coupled imaging algorithm in terms of reconstruction accuracy when dealing with different moisture scenarios and levels.

A. 3-D simulated array measurements and moisture model

To generate the synthetic measurement data from the MWT setup shown in Fig. 2, the 3-D time-domain solver of the commercial software CST Studio Suite is used. The computational domain consists of a porous foam $\Omega_{\text{foam}} = [0, 25] \times [-15, 15] \times [-4, 4]$ cm are surrounded by air Ω_{air} , see Fig. 2. For the air sub-domain, we set $\epsilon'_r = 1$ and $\epsilon''_r = 0$ whereas for the foam the moisture areas and the dry part values are chosen based on the dielectric characterisation data discussed earlier. Antennas are positioned with their open-ended center points located at -15 cm to 15 cm with 5 cm center to center distance along the y -axis. The scattering data is generated in

X-band range and uniformly sampled with a frequency step of 5 MHz and stored in terms of a scattering matrix of size 14×14 ($N = 7$).

Although the moisture shapes can be arbitrary in practical cases but for simplicity of modelling, the wet-spots are given a spherical and cubic shapes with the defined dielectric constant corresponding to the different moisture levels. Here, the dielectric constant value of the foam is known *a-priori* which was determined through the dielectric characterization of the polymer foam using a cavity perturbation technique at room temperature [37]. From the dielectric characterization, the real part of relative dielectric constant was found to be in the range of $1.164 - 3.255$ and imaginary part varying between $0.017 - 0.276$ for *wet basis* moisture content from 0% to 80% , respectively.

B. Inversion algorithm implementation

To obtain the qualitative image using the MUDT, only the diagonal elements and the $S_{(i+1)i}$, ($i = 1, 2, \dots, 6$) of scattering matrix, measured with the top antennas are used in the image reconstruction. Full details of the MUDT implementation are provided in [10].

In the Bayesian framework, we chose the method of moment (MoM) [39] with pulse basis for the forward model, and point-matching testing function. In the forward model, the antennas are modeled as point sources and the electric field data E_{MoM} is converted to equivalent scattering matrix (in terms of S-parameter) S_{MoM} through calibration with respect to dry foam response as

$$S_{\text{MoM}} = \frac{S_{\text{sctdry}}}{E_{\text{MoMdry}}} \odot E_{\text{MoM}}, \quad (20)$$

where S_{sctdry} and E_{MoMdry} are the responses under the dry foam condition, respectively. For the MoM computation, 8.3 GHz frequency point was chosen as it offers less degree of non-linearity than higher frequency points in the X-band [40], [41]. Further, we assume that the imaging domain Ω_{foam} is discretized into $m \times n = 80 \times 20$ uniform rectangular pixels along the y and z -directions, respectively. Here, the pixel size are chosen to be of size $\lambda/6$ so as to achieve sufficient numerical accuracy for the MoM solver. Thus, total number of unknowns in the imaging domain i.e., the real and imaginary part of the dielectric constant, for estimation becomes 3200 . Note that a different solver is chosen for synthetic data generation to ignore “inverse crime” [32]. To start the iteration the value of ϵ_{r_0} is set to the dielectric constant of the dry foam i.e. $\epsilon_{r_0} = 1.16 - 0.01j$ and $\alpha = 0.25$ is set for all the reconstructions. The iterations are terminated, following the stopping criteria $Q(\epsilon_{r_{\ell+1}}) < Q(\epsilon_{r_{\ell}})$ where $Q(\epsilon_{r_{\ell}})$ is the norm term defined in (18). The reconstruction algorithm is implemented in MATLAB 2018b and all computations were performed on a computer with the configuration of 32 GB random access memory, Intel Core(TM) i7-7820HQ central processing unit, and Nvidia Quadro M2200 graphics processing unit.

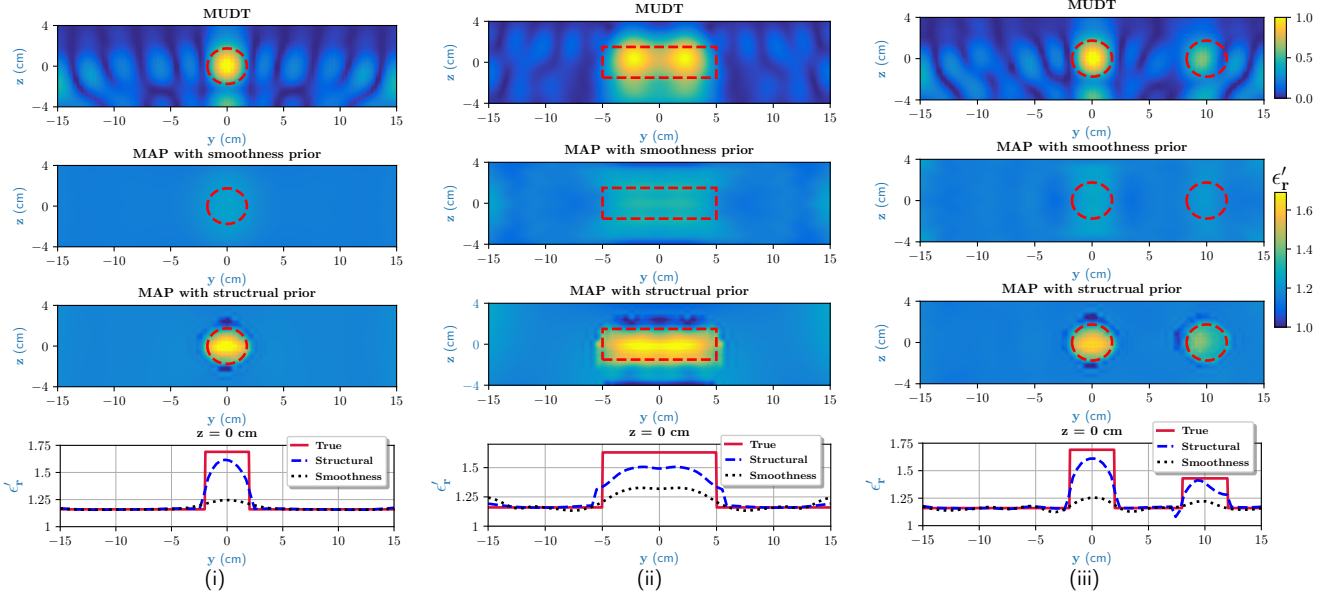


Fig. 4: MUDT and MAP estimates for the (i) one hot-spots case , (ii) piece-wise homogeneous moisture distribution, and (iii) two wet-spots with different moisture case where red dashed shapes indicate the true position of the target. For each case, the bottom figure shows the comparison of MAP with structural and smoothness prior model with the true case for the pixel values located at data line $z = 0$ cm.

C. Noise and error metrics

The noise is added (following [42]) to each response of the complex electric field of the dataset as

$$E_{\text{noise}}^{\text{sct}} = E^{\text{sct}} + \max(E^{\text{sct}}) \frac{\beta}{\sqrt{2}} (\delta_1 + j\delta_2), \quad (21)$$

where $\max(E^{\text{sct}})$ is the absolute maximum value of the scattered electric field, $\delta_1 \sim \mathcal{U}(-1, 1)$ and $\delta_2 \sim \mathcal{U}(-1, 1)$ are two real vectors whose elements are sampled from uniform distribution. The term β denotes the noise level. In all the simulated data, a 3% noise is added which corresponds to $\beta = 0.03$ and SNR of 30 dB. Also, for the noise variances in the MAP computation, Gaussian noise of STD 3% of the peak value of the measurements is considered in both real and imaginary parts of the measurement data.

The reconstruction accuracy has been evaluated by considering the relative reconstruction errors on the contrast function in the imaging domain Ω_{foam} . These errors are measured using the root mean square error (RMSE) percentage and resemblance coefficient (RC). Specifically, the RC is computed as

$$\text{RC}_{\epsilon_r} = \frac{\int \int_{\Omega_{\text{foam}}} \overline{\epsilon_r^{\text{MAP}} \epsilon_r^{\text{True}}} dx dy}{\sqrt{\int \int_{\Omega_{\text{foam}}} (\overline{\epsilon_r^{\text{MAP}}})^2 dx dy} \sqrt{\int \int_{\Omega_{\text{foam}}} (\overline{\epsilon_r^{\text{True}}})^2 dx dy}}, \quad (22)$$

where $\overline{\epsilon_r^{\text{MAP}}} = \epsilon_r^{\text{MAP}} - \langle \epsilon_r^{\text{MAP}} \rangle$, and $\overline{\epsilon_r^{\text{True}}} = \epsilon_r^{\text{True}} - \langle \epsilon_r^{\text{True}} \rangle$, and $\langle \cdot \rangle$ is the mean operator. For the RC, its values vary between 0 and 1. As the RC gets closer to 1, the MAP estimation is closer to the true profile.

D. Imaging scenario

1) *One Dominant wet-spot*: The first scenario is to obtain the location and level of one dominant wet-spot in the polymer foam. Assume a spherical wet-spot with a radius of $0.67\lambda_c$ located at the center of the polymer foam, i.e., (12.5 cm, 0 cm, 0 cm) with 35% moisture level ($\epsilon_r \approx 1.7 - 0.068j$) and surrounded by the dry part. The top figure in Fig. 4 (i) shows the reconstructed image using the MUDT imaging algorithm. As can be perceived from this figure, the location of the wet-spot is correctly obtained with the normalized value of the object function.

To calculate the MAP estimate, information from MUDT with K-means segmentation is used in the structural smoothness prior model. In the structural prior, the CL are set to $c_{y1} = 30$ cm, and $c_{z1} = 8$ cm for the dry part (with very low STD values set for $\sigma_{\epsilon_r'}$, and $\sigma_{\epsilon_r''}$) and for the supported domain of wet-spot, CL of $c_{y2} = 3$ cm, and $c_{z2} = 3$ cm (with STD values set for $\sigma_{\epsilon_r'} = 1$, and $\sigma_{\epsilon_r''} = 0.075$) are chosen. The sigma values in the wet-spots regions are selected based on the dielectric characterisation data and $\pm 3\sigma$ can account for 99% of the dielectric values in the prior from the set mean value of $\eta_{\epsilon_r} = 1.16 - 0.01j$. The aforementioned STD values in both the prior models are used in the remaining cases as well.

Also, we evaluated the MAP estimates with smoothness prior model with a CL of $c_y = 8$ cm, and $c_z = 4$ cm. In the smoothness prior, we set $\sigma_{\epsilon_r'} = 1$, $\sigma_{\epsilon_r''} = 0.075$ and $\eta_{\epsilon_r} = 1.16 - 0.01j$. The MAP estimates with smoothness prior model and structural prior model are shown in Fig. 4 (i). With the smoothness prior, the location of wet-spot is somewhat enlarged and real part of its dielectric value is underestimated. With the structural smoothness prior, MAP

estimate for the real part of the dielectric constant is very close to true case and also the wet-spot is recovered within the correct domain. Further, for easier quantitative comparison, pixel values at data line $z = 0$ cm are compared against the true case and shown in the last figure of Fig. 4 (i). The structural prior follows the discontinuities and aligns closer to the real value than the smoothness prior case. The RC and RMSE values for this case are given in third row of Table I which depicts the accuracy of the structural prior over smoothness prior. In both MAP estimates, imaginary part is overestimated or underestimated and hence not shown. Note that improvement in the image reconstruction is envisaged to be linked to the structural information that is the information of the discontinuities in the solution. Therefore, efforts to study the performance of the MAP solution in respect to different characteristics lengths in the moisture regions are subdued.

2) *Piece-wise homogeneous moisture distribution*: In this scenario, a rectangular distribution for the wet-spot is considered with a moisture content of 30% ($\epsilon_r \approx 1.58 - 0.06j$) and dimension $2.6\lambda_c \times 1.3\lambda_c \times 6.5\lambda_c$ located at the center of the foam. The reconstructed image using MUDT is shown in Fig. 4 (ii). As can be seen from this figure, the exact boundary of the distribution is not reconstructed. Although, the K-means segmentation has resulted in covering a slightly bigger domain.

The MAP estimates are calculated based on the parameter set in the previous case. The results are shown in Fig. 4 (ii). The corners/discontinuities are difficult to estimate with the smoothness prior and more so the estimation shows an irregularity with stretched boundaries and incorrect amount of moisture. As can be seen, the structural prior detects the irregularity and locate it more accurately than the smoothness prior. Overall, its performance is more accurate as evident from line graph in the last figure of Fig. 4 (ii) and the RC and RMSE values for this case as provided in fourth row of Table I. Note that even though the CL in the structural prior are set to the previous case, which does not match with the actual changes, the result is still better.

3) *Wet-spots with different moisture*: In the drying process, i) non-uniform microwave heating during the drying process or ii) non-uniform impregnation, may produce wet-spots with different moisture levels. Hence, in a more pragmatic case, two spherical moisture wet-spots with different moisture levels and with radii of $0.67\lambda_c$ are assumed. The location of the first wet-spot is $(12.5 \text{ cm}, 0 \text{ cm}, 0 \text{ cm})$ with 35% moisture level and the second wet-spot is centered at $(12.5 \text{ cm}, 10 \text{ cm}, 0 \text{ cm})$ with 25% moisture level ($\epsilon_r \approx 1.48 - 0.056j$).

The dominant wet-spot is clearly detected by the MUDT, however, the weaker wet-spot is also visible but not as strong as the other one, as represented by the red dashed circle in top of the Fig. 4 (iii). Following K-means segmentation (not shown here), for the two moisture regions (Ω_{h_1} (middle wet-spot), Ω_{h_2} (right wet-spot)) the CL are set to $c_{y_1} = c_{y_2} = 3 \text{ cm}$, and $c_{z_1} = c_{z_2} = 3 \text{ cm}$. With the smoothness model, it is clear that it can indicate the stronger and weaker wet-spots but with underestimated real part of the dielectric value and over-shaped domain. However, with the structural prior, MAP estimate for the real part of the dielectric constant is very close to true case for the weaker wet-spot and quite close for

TABLE I: RMSE and RC parameter.

Prior	smoothness		structural	
	RMSE	RC	RMSE	RC
Case1: one wet-spot	6.33	0.73	4.23	0.88
Case2: rectangular wet-spot	9.03	0.59	5.57	0.91
Case3: wet-spots (different moisture)	7.40	0.59	4.41	0.90

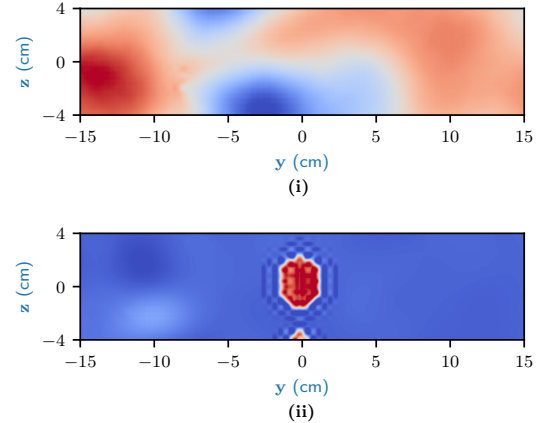


Fig. 5: (i) first singular vectors of the matrix pair (J, L) computed with the smoothness prior, and (ii) first singular vectors of the matrix pair (J, L) computed with the structural prior model.

the stronger wet-spot. Also, both the wet-spots are recovered within the correct domain. Further, to assess the closeness of the estimate from two prior models, pixel values at data line $z = 0$ cm are compared against the true case and shown in the last figure of Fig. 4 (iii). Again, the reconstruction accuracy is better with the combined approach. The corresponding RC and RMSE values are provided in the last row of Table I.

E. GSVD analysis

The reason for improvement in the image quality with structural prior can be analyzed using the generalized singular value decomposition (GSVD) analysis of the pair (J, L) [43] where J is the Jacobian matrix (see (16)) and L is the Cholesky factorisation of the prior covariance matrix. Let $J \in \mathbb{R}^{2S \times 2N_n}$ and $L \in \mathbb{R}^{2N_n \times 2N_n}$ and $\mathcal{N}(J) \cap \mathcal{N}(L)$, where $\mathcal{N}(\cdot)$ is a null space. Then, there exist matrices U and V with the orthonormal columns and non-singular matrix X such that

$$J = U \begin{pmatrix} \Psi & 0 \\ 0 & I_{n-p} \end{pmatrix} X^{-1}, \quad (23)$$

and

$$L = V \begin{pmatrix} \Upsilon & 0 \end{pmatrix} X^{-1}. \quad (24)$$

The term Ψ and Υ are the diagonal matrices that is given as

$$\Psi = \text{diag}(\lambda_1, \lambda_2, \dots, \lambda_p) \quad \text{where} \quad 0 \leq \lambda_1 \leq \lambda_2 \leq \dots \leq \lambda_p,$$

and

$$\Upsilon = \text{diag}(\gamma_1, \gamma_2, \dots, \gamma_p) \quad \text{where} \quad \gamma_1 \geq \gamma_2 \geq \dots \geq \gamma_p \geq 0.$$

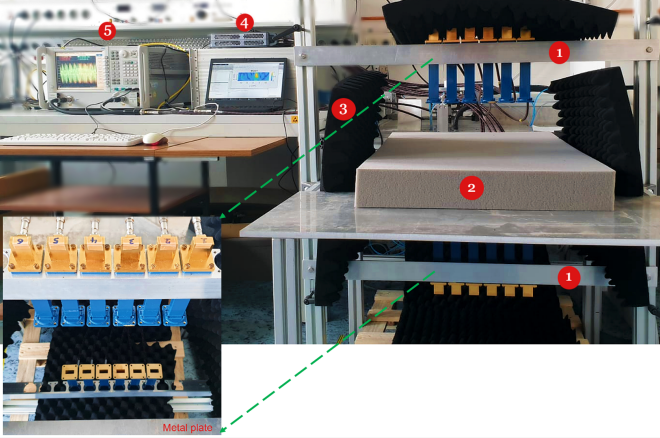


Fig. 6: MWT experimental setup. The MWT system consists of X-band open-ended waveguide antennas as sensors.

The sum of the diagonal matrix must satisfy the relation $\lambda_i^2 + \gamma_i^2 = 1$. Then, the generalised singular values for the matrix pair (J, L) can be defined as

$$\sigma_i = \frac{\lambda_i}{\gamma_i} \quad \forall i = 1, 2, \dots, p \quad (25)$$

The generalised singular values σ_i values appear in non-increasing order and show the ill-posedness of the problem by rapidly decaying to zero with the increasing index. Thus, the role of the matrix pair (J, L) can be understood as to basically regularise the inversion by suppressing the singular vectors associated with the small singular values [14], [44]. The first singular vectors x_i from the smoothness prior model and structural prior model are shown in Fig. 5 (i) and (ii). It can be seen that the smoothness prior presents a smoothing solution everywhere with no sharp discontinuities but the structural prior offers less fluctuations in the dry part and is also discontinuous. It implies that the structural information emerges to having been inserted in the singular vectors x_i .

V. MWT SYSTEM CONFIGURATION AND INVERSION RESULTS

In this section, we evaluate the performance of the developed algorithm on MWT data from our developed MWT system. The testing and validation phase is carried out at laboratory scale in which specific test cases of moisture scenarios are considered inside the foam under static conditions.

A. Imaging domain, antennas, and data acquisition

Figure 6 shows is the prototype MWT setup and its transmitting/receiving 12 WR90 open-ended (Tag 1) waveguide antennas (VSWR 1.03 : 1) connected (with the phase stable cables with phase stability 3° at maximum frequency) to the Agilent N5224A VNA (Tag 5) with a P9164C 2×16 USB Solid state switch matrix (Tag 4). We acquire the back-scattered data from 8 GHz to 12 GHz with frequency step of 5 MHz. It should be noted that a waveguide calibration is performed to remove the unwanted reflections. Communication between the VNA, switch, and the controlling computer

is accomplished through the local area network (LAN). The data acquisition process is entirely automated using MATLAB R2018b. Antennas are resided in semi-infinite free-space from -12.5 cm to 12.5 cm along the y -axis and the distance of the top and bottom antennas to the top and bottom of the polymer foam is 12 cm, and the center to center distance between two adjacent antennas is 5 cm. In addition, absorbers (Tag 3) are placed around the MWT sensor array. To compute the MAP estimate (i) the standard deviations of the measurement noise (see (15)) is calculated for 8.3 GHz frequency point following the approach used in [36], and (ii) scattered electric field of the dry foam case is also measured to perform the calibration steps (see (20)) in order to eliminate multiplicative systematic errors, such as a phase shifts.

B. Foam embedded with one and two wet-spots

To create the one moisture irregularity, a spherical shaped foam of diameter 2.5 ± 0.1 cm and with 45% *wet-basis* moisture level ($\epsilon_r \approx 2.0 - 0.092j$) is chosen and placed inside the foam (see number Tag 2 in Fig. 6) through incision. An approximate location of the irregularity inside the foam is centered at $(0$ cm, -9 cm, 1.55 cm). The image obtained using MUDT is shown in Fig. 7 (i). As can be seen, location of the wet-spots is correctly estimated but with a slightly elongated domain for the wet-spot. More so, the dry and moisture areas are clearly discernible.

From the MUDT image, the structural information is extracted using K-means segmentation (not shown here) and utilised to form the structural prior model in which the CL of $c_{y_1} = 25$ cm, and $c_{z_1} = 7$ cm for the dry part and for the supported domain of wet-spot, CL of $c_{y_2} = 3$ cm, and $c_{z_2} = 3$ cm are chosen. Also, we evaluated the MAP estimates with smoothness prior model only with a CL of $c_y = 8$ cm, and $c_z = 4$ cm. The MAP estimates are shown in middle and last row of Fig. 7 (i). Although the wet-spot is somewhat correctly located in both priors, it is the structural prior that has estimated the moisture levels (represented here in terms of real part of the dielectric constant) more accurately than the smoothness prior solution. In addition, false artifacts are also visible in the MAP solution with smoothness prior. Improvement in the image quality with structural prior can be speculated to be due to suppression of smooth variations in the background (i.e. the dry part).

In the second experiment, we inserted two wet-spots with moisture percentage of 50% ($\epsilon_r \approx 2.2 - 0.1j$) and 45% ($\epsilon_r \approx 1.98 - 0.076j$), respectively. The location of the wet-spot with 50% is centered at $(0$ cm, -3.6 cm, 1.55 cm) and location of the wet-spot with 45% is same as in the previous case. The MUDT image for this case is shown in Fig. 7 (ii). The wet-spot on left is located correctly but a shift is seen for the second irregularity. In the K-mean segmentation, the two regions got merged as the two irregularities are close and share same neighbourhood; it then results in forming a nearly ellipsoid region which is then used in the structural prior. To evaluate the MAP estimate the characteristics length parameters are kept same as in the previous case. From the MAP estimates in Fig. 7 (ii), even though the structural information from segmentation

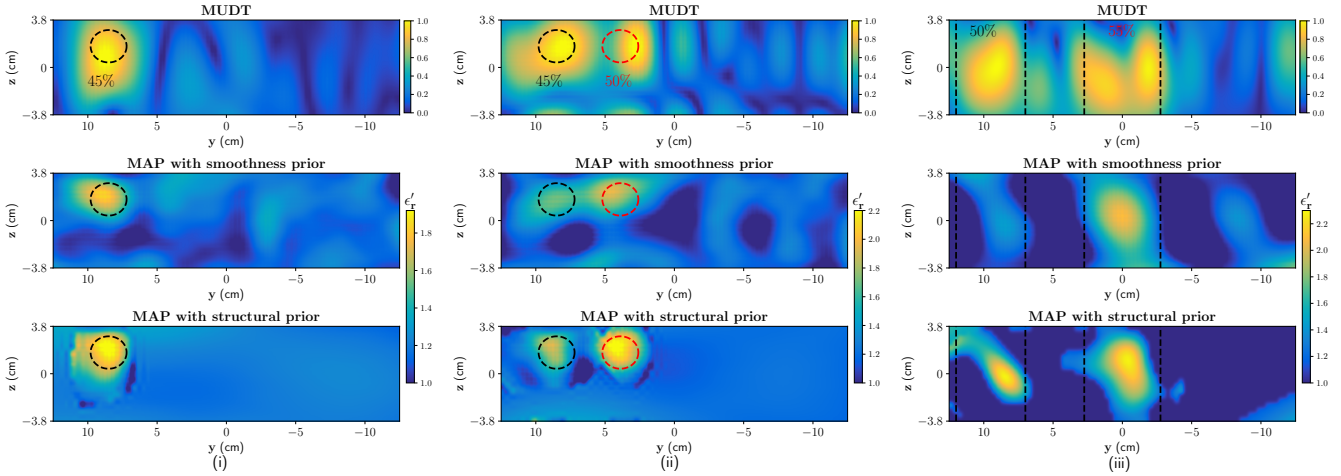


Fig. 7: MUDT and MAP estimates for cases (i) one wet-spot with 45% moisture, (ii) two wet-spots with 45% moisture and 50% moisture, respectively and (iii) moisture in cubic inclusions. The dashed shapes indicate the true positions of the wet-spots.

indicated a wider domain, the two wet-spots are retrieved more accurately than with the smoothness prior.

C. Moisture in cubic inclusions

In this case, two cubic shape pieces are cut out from the foam and infused with moisture levels of 50% ($\epsilon_r \approx 2.2 - 0.1j$) and 55% ($\epsilon_r \approx 2.4 - 0.16j$) in its full volume. After moisture infusion, the respective pieces are placed on the cut out location. The MUDT image for this case is shown in Fig. 7 (iii) in which the inclusion on left is indicating a presence of moisture, though not in full volume, and inclusion in middle indicates a presence of multiple wet-spots. Thus, the localisation information from MUDT is seen to be slightly decreased in this case may be due to limited view and limited independent data. In the structural prior, we have set the same CL in both the moisture regions. From the MAP estimates in Fig. 7 (iii), although the structural information from segmentation was somewhat inaccurate as it includes multiple wet-spots in the middle inclusion, a clear presence of higher moisture is still indicated, though not in full volume, in the MAP solution with structural prior model in comparison to the smoothness based solution that can only locate moisture presence in the middle inclusion. The false solution in the smoothness prior model can be speculated to be due to over-regularisation or smoothing effect. Overall, incorporating structural prior model has improved the accuracy of estimated moisture location and its dielectric properties. We also noticed that even with change in CL to larger values the results show significantly no change.

VI. CONCLUSION AND DISCUSSION

A new coupled MWT imaging method is proposed for obtaining the location of the moisture and their dielectric constant values in the polymer foam. The idea is to improve the reconstruction quality of the Bayesian inversion algorithm by incorporating structural prior information derived from the MUDT qualitative imaging algorithm. The structural smoothness prior model strongly encodes the structural changes inside the foam based on the localisation information from the MUDT. This

way of obtaining structural prior information is effective as it utilizes the data from the same microwave sensor setup in contrast to the priors derived for other imaging modalities or radar-based techniques. The validity of the proposed approach is tested with 3-D synthetic data for pragmatic moisture cases and positively compared with that of solution from smoothness prior. In the final steps, the proposed imaging algorithm is verified with experimental data from the developed MWT setup and results show that there is a significant increase in accuracy and in overall image quality.

We observed a decrease in spatial resolution in range direction when target size greater than maximum achievable spatial resolution [45] were considered. Thus, it can be deduced that with increase in the size of the target the spatial resolution will decrease as caused due to the filtering effects introduced by the scattering operator under Born approximation [46]. Also, with large displacement in the target with respect to the sensor apparatus artifacts are observed in the reconstructed image. Furthermore, in this work, isolated regions of moisture as considered in the numerical and experimental study are likely to occur in practice. These situations arises especially at the outlet stage in the drying process since the foam has been partially dried due to the heating operation. Therefore, beneficial would be to integrate MWT at the outlet rather than inlet to fully justify for the use of structural prior knowledge. Future work will be related to doing dynamic measurements where the foam will be under movement. To further reduce the data acquisition time from MWT sensor setup, limited-view MWT setup has been in testing phase. In general, the proposed method can be extended for the through-the-wall radar imaging (TWRI) applications, ground penetrating radar (GPR) applications and even with the media with rough surfaces.

REFERENCES

- [1] Z. Wu and H. Wang, "Microwave tomography for industrial process imaging: Example applications and experimental results.," *IEEE Antennas and Propagation Magazine*, vol. 59, pp. 61–71, Oct 2017.

- [2] J. A. Tobon Vasquez, R. Scapaticci, G. Turvani, M. Ricci, L. Farina, A. Litman, M. R. Casu, L. Crocco, and F. Vipiana, "Noninvasive inline food inspection via microwave imaging technology: An application example in the food industry," *IEEE Antennas and Propagation Magazine*, vol. 62, no. 5, pp. 18–32, 2020.
- [3] Z. Wu, "Developing a microwave tomographic system for multiphase flow imaging: advances and challenges," *Transactions of the Institute of Measurement and Control*, vol. 37, no. 6, pp. 760–768, 2015.
- [4] J. LoVetri, M. Asefi, C. Gilmore, and I. Jeffrey, "Innovations in electromagnetic imaging technology: The stored-grain-monitoring case," *IEEE Antennas and Propagation Magazine*, vol. 62, no. 5, pp. 33–42, 2020.
- [5] Y. Sun, *Adaptive and Intelligent Temperature Control of Microwave Heating Systems with Multiple Sources*. KIT Scientific Publishing, Karlsruhe, 2016.
- [6] N. Li, G. Link, M. Engler, and J. Jelonek, "Small-size coaxial resonant applicator for microwave heating assisted additive manufacturing," *IEEE Transactions on Microwave Theory and Techniques*, vol. 69, no. 11, pp. 4631–4638, 2021.
- [7] P. L. Jones and A. T. Rowley, "Dielectric drying," *Drying Technology*, vol. 14, no. 5, pp. 1063–1098, 1996.
- [8] A. Martynenko and A. Bück, *Intelligent Control in Drying*. Advances in Drying Science and Technology, CRC Press, 2018.
- [9] A. Omrani, R. Yadav, G. Link, T. Lähivaara, M. Vauhkonen, and J. Jelonek, "An electromagnetic time-reversal imaging algorithm for moisture detection in polymer foam in an industrial microwave drying system," *Sensors*, vol. 21, no. 21, 2021.
- [10] A. Omrani, R. Yadav, G. Link, and J. Jelonek, "A multistatic uniform diffraction tomography algorithm for microwave imaging in multilayered media for microwave drying," *IEEE Transactions on Antennas and Propagation*, May 30, 2022.
- [11] A. Omrani, G. Link, and J. Jelonek, "A multistatic uniform diffraction tomographic algorithm for real-time moisture detection," in *2020 IEEE Asia-Pacific Microwave Conference (APMC)*, pp. 437–439, 2020.
- [12] K. Ren and R. J. Burkholder, "A uniform diffraction tomographic imaging algorithm for near-field microwave scanning through stratified media," *IEEE Transactions on Antennas and Propagation*, vol. 64, no. 12, pp. 5198–5207, 2016.
- [13] S. Sadeghi, K. Mohammadpour-Aghdam, R. Faraji-Dana, and R. J. Burkholder, "A DORT-uniform diffraction tomography algorithm for through-the-wall imaging," *IEEE Transactions on Antennas and Propagation*, vol. 68, no. 4, pp. 3176–3183, 2020.
- [14] A. Borsic, W. Lionheart, and C. McLeod, "Generation of anisotropic-smoothness regularization filters for eit," *IEEE Transactions on Medical Imaging*, vol. 21, no. 6, pp. 579–587, 2002.
- [15] J. P. Kaipio, V. Kolehmainen, M. Vauhkonen, and E. Somersalo, "Inverse problems with structural prior information," *Inverse Problems*, vol. 15, no. 3, pp. 713–729, 1999.
- [16] A. Omrani, R. Yadav, M. Vauhkonen, G. Link, T. Lähivaara, and J. Jelonek, "A combined microwave imaging algorithm for localization and moisture level estimation in multilayered media," in *2021 15th European Conference on Antennas and Propagation (EuCAP)*, pp. 1–5, 2021.
- [17] C. Rasmussen and C. Williams, *Gaussian Processes for Machine Learning*. The MIT Press, 2006.
- [18] P. Meaney, A. Golnabi, N. Epstein, S. Geimer, M. Fanning, J. Weaver, and K. Paulsen, "Integration of microwave tomography with magnetic resonance for improved breast imaging," *Medical physics*, vol. 40, pp. 103101-1–103101-13, Oct. 2013.
- [19] N. Bayat and P. Mojabi, "Incorporating spatial priors in microwave imaging via multiplicative regularization," *IEEE Transactions on Antennas and Propagation*, vol. 68, no. 2, pp. 1107–1118, 2020.
- [20] A. H. Golnabi, P. M. Meaney, and K. D. Paulsen, "Tomographic microwave imaging with incorporated prior spatial information," *IEEE Transactions on Microwave Theory and Techniques*, vol. 61, no. 5, pp. 2129–2136, 2013.
- [21] D. Kurrant, A. Baran, J. LoVetri, and E. Fear, "Integrating prior information into microwave tomography part 1: Impact of detail on image quality," *Medical Physics*, vol. 44, no. 12, pp. 6461–6481, 2017.
- [22] D. Kurrant and E. Fear, "Defining regions of interest for microwave imaging using near-field reflection data," *IEEE Transactions on Microwave Theory and Techniques*, vol. 61, no. 5, pp. 2137–2145, 2013.
- [23] F. M. Saraskanroud and I. Jeffrey, "A comparison of time-domain and frequency-domain microwave imaging of experimental targets," *IEEE Transactions on Computational Imaging*, vol. 7, pp. 611–623, 2021.
- [24] F. Mahdinezhad Saraskanroud and I. Jeffrey, "Hybrid approaches in microwave imaging using quantitative time- and frequency-domain algorithms," *IEEE Transactions on Computational Imaging*, pp. 1–1, 2022.
- [25] N. Abdollahi, I. Jeffrey, and J. LoVetri, "Improved tumor detection via quantitative microwave breast imaging using eigenfunction-based prior," *IEEE Transactions on Computational Imaging*, vol. 6, pp. 1194–1202, 2020.
- [26] I. Catapano, L. Crocco, M. D'Urso, and T. Isernia, "On the effect of support estimation and of a new model in 2-d inverse scattering problems," *IEEE Transactions on Antennas and Propagation*, vol. 55, no. 6, pp. 1895–1899, 2007.
- [27] W. C. Chew, *Waves and Fields in Inhomogeneous Media*. IEEE Press, 1995.
- [28] W. Chew and Y. Wang, "Reconstruction of two-dimensional permittivity distribution using the distorted born iterative method," *IEEE Transactions on Medical Imaging*, vol. 9, no. 2, pp. 218–225, 1990.
- [29] D. G. Dudley, *Mathematical foundations for electromagnetic theory*. IEEE press New York, 1994.
- [30] C. T. Tai, *Dyadic Green's functions in electromagnetic theory*. IEEE Press, 1994.
- [31] R. Yadav, A. Omrani, G. Link, M. Vauhkonen, and T. Lähivaara, "Correlated sample-based prior in bayesian inversion framework for microwave tomography," *IEEE Transactions on Antennas and Propagation*, vol. 70, no. 7, pp. 5860–5872, 2022.
- [32] J. Kaipio and E. Somersalo, *Statistical and Computational Inverse Problems*. Springer-Verlag, 2005.
- [33] R. Autieri, G. Ferraiuolo, and V. Pascazio, "Bayesian regularization in nonlinear imaging: Reconstructions from experimental data in nonlinearized microwave tomography," *IEEE Transactions on Geoscience and Remote Sensing*, vol. 49, no. 2, pp. 801–813, 2011.
- [34] S. Caorsi, G. L. Gragnani, S. Medicina, M. Pastorino, and G. Zunino, "Microwave imaging based on a markov random field model," *IEEE Transactions on Antennas and Propagation*, vol. 42, no. 3, pp. 293–303, 1994.
- [35] A. Franchois and C. Pichot, "Microwave imaging-complex permittivity reconstruction with a Levenberg-Marquardt method," *IEEE Transactions on Antennas and Propagation*, vol. 45, no. 2, pp. 203–215, 1997.
- [36] C. Eyraud, A. Litman, A. Hérique, and W. Kofman, "Microwave imaging from experimental data within a Bayesian framework with realistic random noise," *Inverse Problems*, vol. 25, no. 2, p. 024005, 2009.
- [37] S. Soldatov, T. Kayser, G. Link, T. Seitz, S. Layer, and J. Jelonek, "Microwave cavity perturbation technique for high-temperature dielectric measurements," in *2013 IEEE MTT-S International Microwave Symposium Digest (MTT)*, pp. 1–4, 2013.
- [38] R. Yadav, A. Omrani, M. Vauhkonen, G. Link, and T. Lähivaara, "Microwave tomography for moisture level estimation using Bayesian framework," in *2021 15th European Conference on Antennas and Propagation (EuCAP)*, pp. 1–5, 2021.
- [39] J. Richmond, "Scattering by a dielectric cylinder of arbitrary cross section shape," *IEEE Transactions on Antennas and Propagation*, vol. 13, no. 3, pp. 334–341, 1965.
- [40] R. Yadav, A. Omrani, G. Link, M. Vauhkonen, and T. Lähivaara, "Microwave tomography using neural networks for its application in an industrial microwave drying system," *Sensors*, vol. 21, no. 20, 2021.
- [41] O. M. Bucci, N. Cardace, L. Crocco, and T. Isernia, "Degree of nonlinearity and a new solution procedure in scalar two-dimensional inverse scattering problems," *J. Opt. Soc. Am. A*, vol. 18, pp. 1832–1843, Aug 2001.
- [42] A. Abubakar, P. van den Berg, and S. Semenov, "A robust iterative method for born inversion," *IEEE Transactions on Geoscience and Remote Sensing*, vol. 42, no. 2, pp. 342–354, 2004.
- [43] P. Hansen, *Rank-Deficient and Discrete Ill-Posed Problems: Numerical Aspects of Linear Inversion*. Monographs on Mathematical Modeling and Computation, Society for Industrial and Applied Mathematics (SIAM, Philadelphia), 1998.
- [44] Q. Fang, P. Meaney, and K. Paulsen, "Singular value analysis of the jacobian matrix in microwave image reconstruction," *IEEE Transactions on Antennas and Propagation*, vol. 54, no. 8, pp. 2371–2380, 2006.
- [45] A. Naghibi and A. R. Attari, "Near-field radar-based microwave imaging for breast cancer detection: A study on resolution and image quality," *IEEE Transactions on Antennas and Propagation*, vol. 69, no. 3, pp. 1670–1680, 2021.
- [46] G. Gennarelli and F. Soldovieri, "The effect of array configuration in transmission-mode electromagnetic imaging," *IEEE Transactions on Antennas and Propagation*, vol. 62, no. 10, pp. 5148–5156, 2014.